Science Arts & Métiers (SAM)
is an open access repository that collects the work of Arts et Métiers Institute of Technology researchers and makes it freely available over the web where possible.

This is an author-deposited version published in: https://sam.ensam.eu
Handle ID: .http://hdl.handle.net/10985/10521

To cite this version :

Thierry PALIN-LUC, Dominique COUPARD, Christian DUMAS, Philippe BRISTIEL - Simulation of multiaxial fatigue strength of steel component treated by surface induction hardening and comparison with experimental results - International Journal of Fatigue - Vol. 33, n°8, p.1040–1047 - 2011

Any correspondence concerning this service should be sent to the repository
Administrator : scienceouverte@ensam.eu

Simulation of multiaxial fatigue strength of steel component treated by surface induction hardening and comparison with experimental results

T. Palin-Luc [a,*], D. Coupard [a], C. Dumas [b], P. Bristiel [c]

[a] *Arts et Métiers ParisTech, I2M, UMR CNRS, Esplanade des Arts et Métiers, F-33405 Talence Cedex, France*
[b] *Renault, Technocentre, DIMat, TCR LAB 035, 1 Av. du Golf, 78288 Guyancourt Cedex, France*
[c] *Prisméca, 191 Av. du Général Leclerc, 78220 Viroflay, France*

Keywords:
High-cycle fatigue
Multiaxial fatigue
Surface induction hardening
Residual stresses
Crack initiation

ABSTRACT

This paper proposes a method to assess the high-cycle multiaxial fatigue strength of components treated by surface induction hardening (SIH). Surface quenching following surface induction heating is simulated, taking into account the following features of the process: (i) electromagnetic and thermal fields, (ii) phase transformation, and (iii) the residual stress field resulting from the entire process. The fatigue strength of the specimens was simulated using Crossland and Dang-Van criteria; the field of the residual stresses and the fatigue characteristics of both the untreated material and the treated layer (martensite) are considered. Fatigue tests on smooth specimens were carried out to compare simulated results with experimental data. These tests yield information regarding the influence of the thermal treatment on material behaviour and strength, including microstructure evolution and mechanical characteristics, especially in fatigue. For this purpose, residual stresses were analyzed by X-ray diffraction before and after the fatigue tests. Fatigue crack initiation areas (at the specimen's surface or below) are predicted depending on the depth of the hardened material layer. The simulation of the fatigue strength at 2×10^6 cycles is in good agreement with experimental results.

1. Introduction

For ecological and economic reasons, the automotive industry must reduce the weight and fuel consumption of vehicles. Consequently, the performance of engine components must be improved to allow them to withstand increasing mechanical loads. The current tendency is to substitute using carbon steels, for which fatigue strength must be increased by an optimised reinforcement treatment. Surface induction heating followed by quenching is one such treatment. One of the main features of surface induction hardening (SIH) is its large fatigue strength improvement [1]. This is also a cleaner process because it uses less toxic products than used in carburizing or nitriding.

Surface induction hardening gives rise to a tough core, having tensile residual stresses, and a hard surface layer, having compressive stresses, in the component [2]. This configuration has proven to be very efficient for increasing fatigue strength [3,4]. However, the effectiveness of residual stresses is quite dependent on their distribution in the component and on their relaxation (if any) during in-service fatigue loading. Depending on both the field of residual stresses and the applied external fatigue loading, cracks can either initiate in the vicinity of the surface or beneath the hardened layer [5]. The great importance of residual stresses to the fatigue strength of materials and structures is now well known.

The aim of this paper is to present a complete methodology to simulate the effect of the SIH reinforcement process on the multiaxial fatigue strength of steel components, taking into account the multiaxial nature of both the field of residual stresses and the field of stresses due to cyclic mechanical loading. Optimisation of such a surface treatment in a design department will then be possible for a given component.

Two depths of heat-treated material are studied and their properties (metallurgy and residual stresses) are compared to the base material's properties. A testing fatigue plan was built to evaluate the influence of the depth of heat-treated material on the fatigue behaviour. Finally, a simulation of the entire process has been developed and its results compared to experimental analysis of residual stresses. The proposed methodology to evaluate the multiaxial fatigue strength has been validated. Data obtained in this study are used by engineers to simulate the mechanical behaviour of components and to prevent fatigue failure.

---

[*] Corresponding author.

E-mail addresses: thierry.palin-luc@ensam.eu (T. Palin-Luc), christian.dumas@renault.com (C. Dumas).

Nomenclature

a, b	material parameters of the Crossland criterion
$\vec{B}$	magnetic induction
$\vec{E}$	electric field
E	Young modulus
$\vec{H}$	magnetic field
$\vec{J}$	electric current density
$\underline{n}$	unit normal vector orienting the material plane under consideration
P_e	electromagnetic power density dissipated into the workpiece
R	nominal stress ratio
$Rp_{0.2}$	yield stress with 0.2% plastic strain
Rm	maximum tensile strength
t	time

α, β	material parameters of the Dang Van criterion
$\Delta\sigma_{nom}$	nominal stress range
ρ	mass density
$\Sigma_{H,\max}$	maximum hydrostatic stress over a load cycle
σ_H	mesoscopic hydrostatic stress
σ^D_{pb}	fatigue strength at 2×10^6 cycles under fully reversed plane bending
$\sigma^D_{rotbend}$	fatigue strength at 2×10^6 cycles under fully reversed rotating bending
τ^D	fatigue strength at 2×10^6 cycles under fully reversed torsion
τ	mesoscopic shear stress vector
$\tau_{oct,amp}$	octahedral shear stress amplitude

2. Experiments

2.1. Base material and specimens

This study has been carried out on smooth cylindrical specimens (Fig. 1) with a theoretical stress concentration factor of 1.02 in bending [6]. These specimens were machined from round cold-rolled bars of the low-alloyed carbon steel D38MnV5S. The chemical composition of this steel is shown in Table 1, its quasi-static mechanical characteristics under monotonic tension before any SIH treatment ("untreated material") are given in Table 2. Three sets of specimens were tested: (a) base material, i.e. untreated specimens with a normalised microstructure, (b) heat-treated specimens with an induction hardened depth of approximately 2 mm ("medium depth"), (c) induction heat-treated specimens with a hardened depth of approximately 3 mm ("large depth"). The untreated material has a normalised ferritic–pearlitic microstructure (Fig. 2a). Some elliptic MnS inclusions surrounded by a thin alumina layer were observed (Fig. 2b).

Table 1
Chemical composition (wt.%) of the D38MnV5S steel.

C	Mn	Si	Al	S	V+Nb	Cr	Cu	Mo	Sn
0.35	1.23	0.59	0.032	0.065	0.09	0.21	0.2	0.078	0.012

Table 2
Mechanical characteristics of the D38MnV5S steel under quasi-static monotonic tension.

E (GPa)	ν	$Rp_{0.2}$ (MPa)	Rm (MPa)	HV
227	0.3	538	811	300

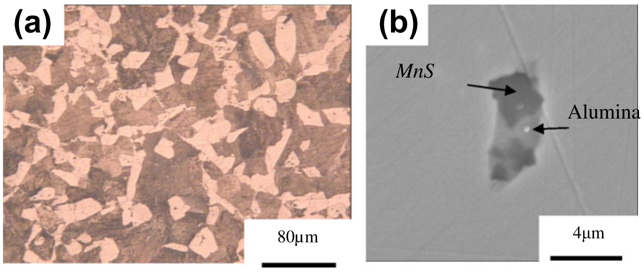

Fig. 2. (a) Microstructure of the untreated material and (b) MnS and alumina inclusions.

2.2. Induction process and heat treatment

The induction surface treatment was carried out with a 20 kHz induction furnace and a one-turn coil. The heating power was 190 kW throughout. The total heating time was 1.2 s for the first set of treated specimens (b), and 1.6 s for the second one (c). After induction heating, the water quenching was started, with a delay of 0.5 s. Thereafter, all the treated specimens (sets b and c) were tempered at 180 °C for 1 h 30 min in a furnace with inert gas. The microstructure of the treated specimens is detailed in [10]. For batch (b), the microstructure is mainly martensitic with a small volume fraction of ferrite down to a depth of 2.5 mm. Beyond 2.5 mm (in the core), the initial ferrite pearlite microstructure is not affected by SIH. According to a hardness criterion of 500 HV, the hardened layer has a depth of 2 mm, as illustrated in Fig. 3 [10]. The specimens of batch (c) have an SIH layer with a larger depth: up to 3 mm, according to the previous hardness criterion.

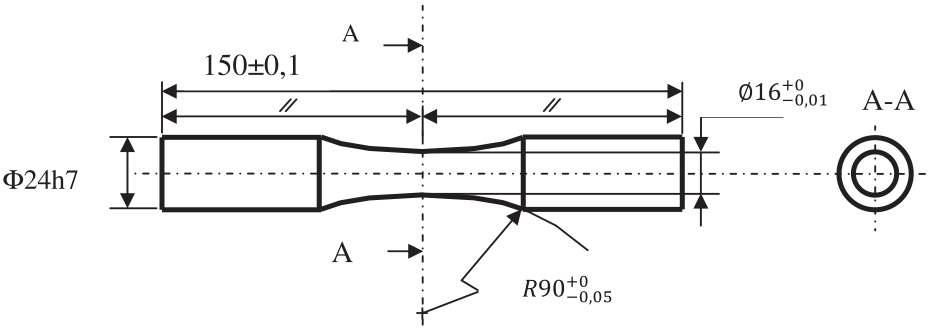

Fig. 1. Specimen geometry (Kt = 1.02 in bending).

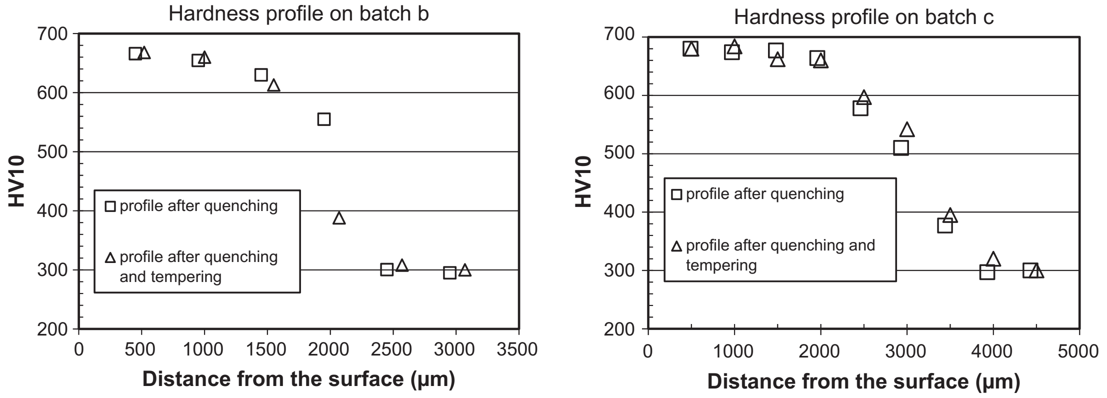

Fig. 3. Hardness profile for the two batches (b) and (c).

There is no ferrite below the surface to 1 mm, and there is a small volume fraction between 1 mm and 4 mm (see [10] for details).

2.3. Fatigue test conditions

All the fatigue tests were carried out under load control, on a resonant (four-point) plane bending fatigue testing machine (Fig. 4a) at a frequency of 50 Hz using the stair-case method, in order to determine the fatigue strength of the specimens at 2×10^6 cycles. A schematic of the fatigue testing machine is given in Fig. 4b. The cylindrical specimen (1) is gripped by collets. It is embedded at one end in the machine frame, which is equipped with bending moment sensors with strain gauges (2). The other end of the specimen is gripped by a long arm (7). This arm is loaded vertically by a sinusoidal vertical force generated by an electromagnetic shaker (5). The specimen is seen by the electronic control system as a spring loaded in bending without shear force (pure bending). The electronic system controls the amplitude and the mean value of the bending moment and ensures that the loading is at the resonant frequency of the machine. This frequency can be adjusted via a mass (3) and a spring (4). Due to the long length of the arm (7), $L = 300$ mm, the tension compression stress applied on the specimen is less than 1% of the bending stress, and thus, can be neglected. A stepper motor (6) applies the mean (static) bending moment to the specimen by moving the frame of the actuator.

For the untreated specimens, the fatigue strength was determined both under fully-reversed loading ($R = -1$) and under constant maximum nominal stress $\sigma_{nom,\max} = 770$ MPa (the nominal stress range $\Delta\sigma_{nom}$ varied in a stair-case from one specimen to another). For the treated specimens, only the fully-reversed fatigue strength in-plane bending was determined. Each fatigue strength was determined using 15 specimens (Table 3). The tests were stopped when the resonant frequency decreased by more than 2% of its initial frequency (i.e. the frequency at the beginning of the fatigue test when the specimen was undamaged). This corresponds to a crack of several millimeters, as shown in Fig. 5.

Table 3 shows that the fatigue strength at 2×10^6 cycles is magnified by a factor of $\sim$1.3 for the specimens heat-treated at a depth of 2 mm and by more than 1.46 for treatment at the large depth (3 mm).

2.4. X-ray residual stress analysis

Residual stress analysis was conducted by X-ray diffraction (XRD) according to the French standard AFNOR XP A 09-285 [7–9]. The classical “sin2 ψ” method was applied for stress evaluation with the use of at least 11 ψ angles for each stress value. The analysis zone is limited by a collimator of 1 mm in diameter. A “SET-X” XRD apparatus was used which consisted of an X-ray generator; a PC microprocessor; a goniometric head equipped with a ELPHYSE position sensitive detector; a stress analysis software package (SET-X and STERESS-AT) licensed to Arts et Métiers ParisTech and commercialised by Elphyse and Siemens. XRD analysis was carried out in martensite or/and ferritic phase with Chromium Kα radiation and {211} plans. The used elastic constants for stress evaluation were: ½ $S_{2\{211\}} = 5.83 \times 10^{-6}$ MPa^{-1}, $S_{1\{211\}} = -1.28 \times 10^{-6}$ MPa^{-1}. The obtained precision on stress analysis is better than 50 MPa, which represents a divergence from linearity and is

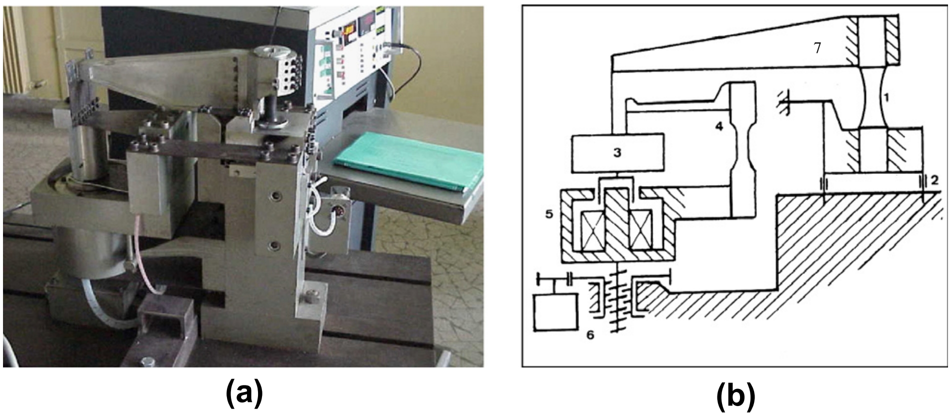

Fig. 4. (a) Plane bending fatigue testing machine and (b) scheme of its principle.

Table 3
Experimental fatigue strength at 2×10^6 cycles.

Specimen set	$R = \sigma_{\min}/\sigma_{\max}$	$\Delta\sigma^D_{nom}/2$ (MPa)	Standard deviation (MPa)
Untreated material (a)	-1	410	~25
Untreated material (a)	$R \sim 0.1$, $\sigma_{nom,\max} = 770$ MPa	370	~25
Treated at medium depth (b)	-1	527	20
Treated at large depth (c)	-1	>600[a]	38

[a] The experimental fatigue strength of the specimens treated at large depth (c) is not significant because after the end of the fatigue test, some cracks were observed in the parts of the specimen which are clamped in the machine grips. This is discussed later. In fact, for these specimens with fatigue crack outside the median torus (testing area), no other crack were observed in the testing area (with a diameter of 16 mm). This means that the real fatigue strength for this specimen set is higher than the experimental result of 600 MPa.

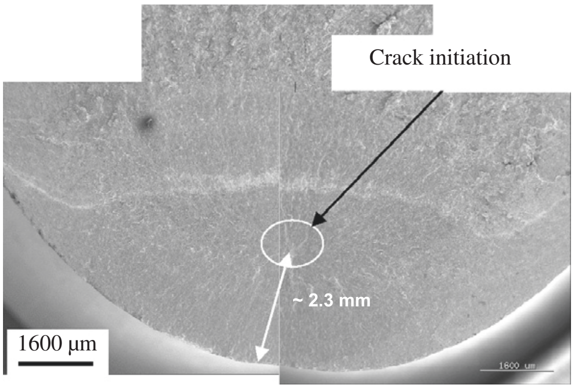

Fig. 5. Fracture surface of an induction-hardened specimen at medium depth (~2 mm) after plane bending fatigue test at a fatigue strength $\Delta\sigma^D_{nom}/2$ = 527 MPa.

derived from a test of the validity of the current method in taking into account a 35% error in the manipulation of the apparatus. Due to the weak penetration depth of X-ray radiation into the specimen (about 5 μm with 66% absorption of incident radiation), the measurements in the sub-layer of specimens were carried out after local (6 mm × 6 mm) or circumferential (with 20 mm in length) electrolytic polishing (details are given in [10]). The solution used was a Chlorine-based acid electrolyte. The removal speed was approximately 0.5 μm/s at 50 V and 0.5 A cm^{-2}.

Two material removal techniques were used: local and circumferential electrochemical polishing (at the smallest cross section of the median torus of the specimens). Local material polishing is a fast technique compared to the circumferential material removal technique. It has been shown in the literature [11] that the XRD results recorded after using the local polishing method can be considered valid when the removal depth is less than one tenth of the diameter of the cylindrical specimen. Beyond this value, the results should be corrected to take into account the stress relaxation resulting from local material removal. To the knowledge of the authors, there is no reliable correction model available for this local removal technique. This means that the only option is to use the well-known Moore and Evans correction [11] developed for uniform material removal on a plane specimen. In this case, the reliability of the corrected result is doubtful. Circumferential polishing is a relatively slow technique, for which a correction model is also needed. In that case, the Moore and Evans model is known to overestimate the correction, which means that the true residual stresses must be assumed to be between the uncorrected and corrected results, especially at depths of up to one tenth of the specimen diameter. For larger depths, the reliability of the correction is not known. An interesting aspect of the Moore and Evans correction model is that it gives an estimation of the normal radial stress, something which cannot be directly deduced from experimental analysis. The existence of this normal radial stress below the heat-treated specimen's surface is undeniable from a mechanical point of view, and this is very important for a good estimation of the hydrostatic stress, which is of prior importance in the fatigue crack initiation phenomenon, as described below.

3. Surface induction hardening simulation

3.1. Modelling of the heat treatment

As detailed in [10], the finite element software FLUX 2D®, which is able to solve coupled magneto-thermal problems, has been used to estimate the evolution of the power density and temperature during the induction heating process. This is done by solving Maxwell's equations in a stationary state and considering two additional constitutive equations [10]. Solving these equations enables one to determine the magnetic field $\vec{H}$, the magnetic induction $\vec{B}$, the electric field $\vec{E}$, and the electric current density $\vec{J}$. The electromagnetic power density dissipated into the workpiece is then given by: $P_e = (\vec{E} \cdot \vec{E})/\rho_e$. The power density is then integrated directly, inside the heat relation, through the term $\dot{q}$ so as to estimate the thermal field at each heating step. After heating, FLUX 2D® is used to estimate the spatial and temporal evolution of the temperature during quenching. The heat equation is thus solved by considering (1) a convection boundary limit at the free surface of the sample, (2) the evolution of the material's thermal conductivity and specific heat with temperature. At each step of the cooling process, the phase and hardness distribution inside the sample are calculated with the METAL7® software, using the thermal patterns previously estimated with FLUX 2D®. The model is based on the principle of additivity and uses the Johnson–Mehl–Avrami and Koïstinen–Marburger laws to estimate metallurgical transformations and their intensity during cooling from the austenitic temperature to ambient temperature. The thermal and phase distributions during quenching are then added into the finite element MSC MARC® software, so as to estimate the residual stress fields. The model requires the mechanical properties of each phase with respect to their temperature of formation and considers that (i) each macroscopic mechanical property obeys a linear mixture law, (ii) the material obeys the Von-Mises plasticity criterion, (iii) the material's mechanical behaviour is thermo-elastic and perfectly plastic, (iv) the hardening behaviour of the material is isotropic, and (v) the total strain tensor is given by a sum of four tensors: a thermal strain, an elastic strain, a plastic strain, and a transformation strain.

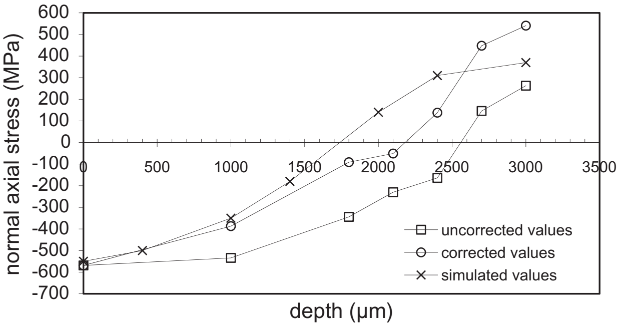

Fig. 6. Corrected (measurements corrected), uncorrected (measured values), and simulated (calculated values) normal axial (σ_{zz}) residual stress profiles for an induction-treated specimen with a hardening depth ~2 mm.

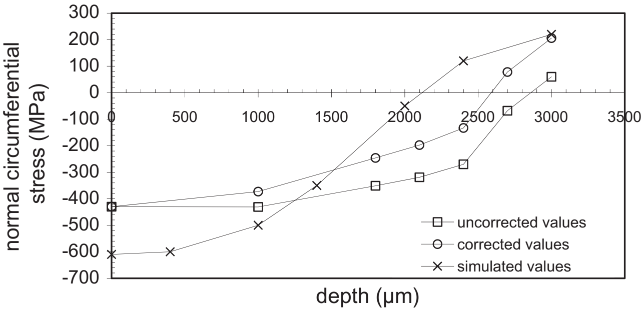

Fig. 7. Corrected (measurements corrected), uncorrected (measured values), and simulated (calculated values) normal circumferential ($\sigma_{\theta\theta}$) residual stress profiles for an induction-treated specimen with a hardening depth ~2 mm.

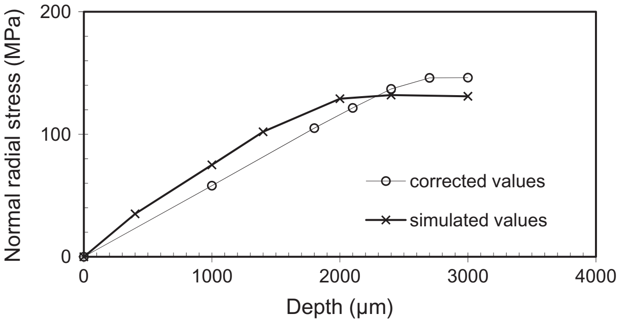

Fig. 8. Normal radial (σ_{rr}) residual stress profiles from experimental analysis corrected by Moore/Evans and from simulation (calculated values).

3.2. Comparison between simulation and experiment

Figs. 6–8 show the axial σ_{zz}, circumferential $\sigma_{\theta\theta}$, and radial σ_{rr}, residual stress profiles for specimens hardened at a depth of approximately 2 mm (set b). X-ray analysis was conducted after local electrochemical polishing and the results are presented (with and without the Moore and Evans correction) together with the simulated residual stresses. Details concerning experimental residual stress analysis and simulations can be found in Ref. [10].

As shown in Figs. 6 and 7, for both normal stresses, σ_{zz} and $\sigma_{\theta\theta}$, the residual stress field is compressive over the two first millimetres, and then becomes tensile. The maximum compressive stress is quite small in surface area compared to the possible compressive stress that this kind of SIH treatment can generate in a similar kind of steel [1]. This might result from natural tempering occurring during quenching below MS (martensite starting). The Moore and Evans correction leads to a tensile normal radial residual stress, σ_{rr}, with a maximum value of approximately 150 MPa (Fig. 8); this is in very good agreement with the simulation results. This shows that the residual stresses are multiaxial below the specimen's surface. If the measurement uncertainties are considered (less than ±50 MPa), the best agreement between experiments and simulation for σ_{zz} and $\sigma_{\theta\theta}$ is obtained when applying the Moore and Evans correction. In this case, simulated and experimental results are in good agreement until approximately one tenth of the specimen diameter, i.e. 1.6 mm.

4. Fatigue strength assessment method

4.1. Fatigue strength modelling

The fatigue strength assessment of specimens treated by surface induction hardening was carried out based on the following assumptions. (i) The specimen is considered a two-material structure: the base material and the martensitic heat-treated zone. (ii) The stabilized residual stresses after relaxation due to cyclic loading are superimposed on the stresses due to mechanical cyclic loading. (iii) Two high-cycle multiaxial fatigue criteria, Dang Van [12] and Crossland [14], are assumed to be representative of the high-cycle multiaxial fatigue crack initiation phenomenum in the specimens. Both are applied and their results are compared below.

At a point M, the Dang Van criterion (1) depends on the amplitude of the mesoscopic shear stress vector $\|\underline{\tau}(M,t,\underline{n})\|$ acting on the material plane oriented by the unit normal vector n and on the mesoscopic hydrostatic pressure $\sigma_H(M,t)$. The two material parameters α and β can be identified from two fatigue strengths on smooth specimens under different loadings or different stress ratios. In this study, for the base material (a) these parameters were identified from the two fatigue strengths indicated in Table 3.

$$\max_{\underline{n}}[\max_{t}(\|\underline{\tau}(M,t,\underline{n})\| + \alpha\sigma_H(M,t))] \leqslant \beta \qquad (1)$$

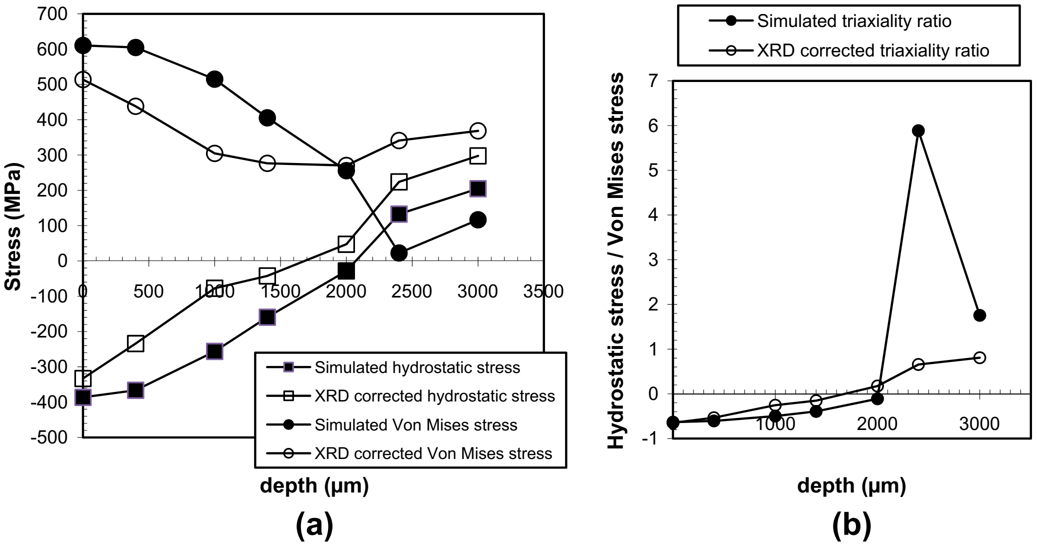

Fig. 9. For an induction-treated specimen with a hardening depth ~2 mm (batch b), (a) hydrostatic stress and Von Mises equivalent stress due to residual stresses and (b) trixiality ratio of residual stresses, both from simulation and experimental XRD analysis corrected by Moore/Evans.

The Crossland criterion is based on a linear combination of the amplitude of the octahedral shear stress amplitude $\tau_{oct,a,\Delta J_2}(M)$ and the maximum hydrostatic stress $\Sigma_{H,\max}(M)$ per load cycle (2). For the base material, the two material parameters *a* and *b* are identified from the two fatigue strengths in Table 3.

$$\tau_{oct,a,\Delta J_2}(M) + a\Sigma_{H,\max}(M) \leqslant b \tag{2}$$

Due to the high brittleness of the martensite, fatigue tests on full martensitic specimens were impossible. Consequently, the fully-reversed fatigue strengths at 2×10^6 cycles under torsion τ^D and plane bending σ_{pb}^D of the martensite were estimated from the maximum compression strength Rm_c of the martensite using the following empirical relations from CETIM [13]. The fatigue strength in pure rotating bending is related to the maximum tensile strength by: $\sigma_{rotbend}^D \approx R_m\,(0.56\text{–}1.4 \times 10^{-4} \times R_m)$. Since the martensite layer in the specimen is in compression due to the residual stresses, the maximum compressive strength has been used as opposed to the maximum tensile strength. To identify this characteristic, quasi-static compression tests were carried out on tubular cylindrical specimens (21 mm long, 13 mm inner diameter, 15 mm outer diameter) machined from the same steel [10]. These specimens were furnace heat-treated (180 °C, 1 h 30 min) to yield a martensitic tempered microstructure. After tempering, the hardness of the cylindrical specimens was similar to that measured in the fatigue specimens which confirms that natural tempering occurred during the quenching of the specimens (after induction surface heating).

4.2. Residual stresses

The stable values of the residual stresses after relaxation were considered static stresses superimposed on the stresses due to cyclic mechanical loading (plane bending in this study). Experimental XRD residual stress analysis on uncracked specimens (one from batch b, one from batch c) after cyclic loading at the fatigue strength for 2×10^6 cycles did not show any relaxation of residual stresses [10]. It is very important to note that the complete tensor of residual stresses is considered in the fatigue strength assessment due to the major role the hydrostatic stress plays in the fatigue crack initiation process [14]. Indeed, it has already been shown that the residual stresses are multiaxial, which is illustrated in Fig. 9, where the triaxiality ratio (hydrostatic stress over Von

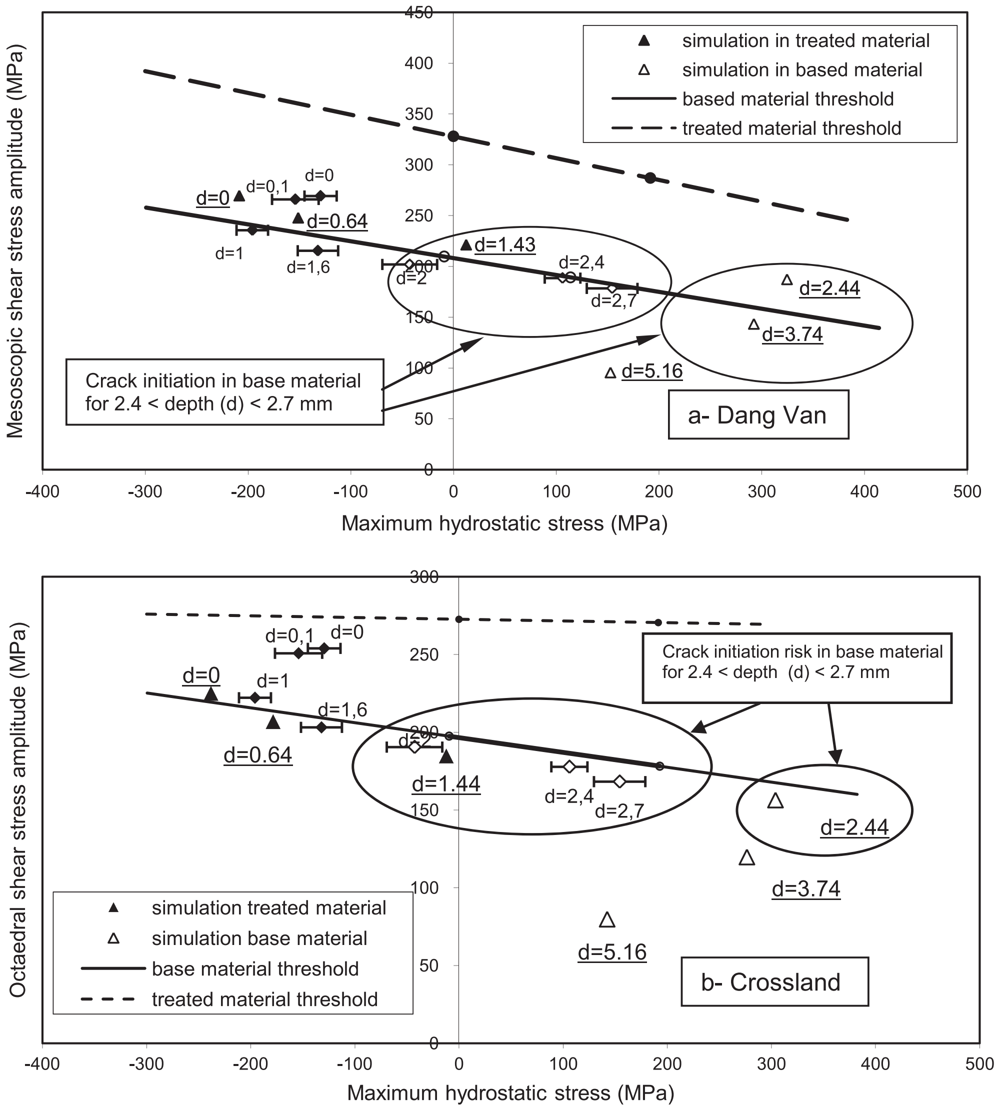

Fig. 10. (a) Dang Van and (b) Crossland diagrams, for the induction surface hardened specimens at medium depth (~2 mm, set b) with residual stresses both from X-ray analysis (♦, ◇) and from simulation (▲, △), under fully reversed plane bending at the fatigue strength $\Delta\sigma_{nom}^D/2 = 527$ MPa. Horizontal bars illustrate the uncertainty due to XRD analysis uncertainty.

Mises equivalent stress) is plotted versus depth. This ratio is at its maximum in the core of the specimen from batch b.

4.3. Comparison between simulation and experiment

Fig. 10 illustrates, for specimens treated at medium depth (~2 mm), the application of the proposed methodology with two criteria (Crossland and Dang Van) at different depths (d in mm) below the specimen surface. This figure shows two sets of points. First, the points representing the cyclic stresses at different depths using the experimental residual stresses recorded by XRD. Second, those from numerical simulation only (points labelled d [underlined]). For these simulations, the stresses due to cyclic loading were computed with an elastic hypothesis and the residual stresses were computed by a finite element analysis of the entire induction process [10].

It is clear from Fig. 10 that for the two criteria, the proposal does not predict any fatigue crack initiation in the treated material since all the points are below the dashed line that represents the fatigue strength of the martensite at 2×10^6 cycles. The difference between Crossland and Dang Van results is not significant. However, the points representative of depths greater than 2 mm (open symbols) have to be compared with the solid line, which corresponds to the threshold of the base material (untreated, in the core). It can be seen that, in both cases (calculated with experimental residual stresses or with simulated residual stresses), fatigue crack initiation before 2×10^6 cycles should occur at depths between 2.4 and 2.7 mm.

This assessment is in very good agreement with the observed crack initiation area on the specimen fracture surface (Fig. 5). Such observations were carried out on all specimens. After the fatigue tests, the specimens were submerged in liquid nitrogen, and were thereafter broken by shock to open the natural fatigue cracks. The same methodology was used to compute the fatigue strength of the specimens treated at large depth (~3 mm). In this case, as previously explained, the experimental fatigue strength in-plane bending ($R = -1$) is unknown, but is higher than 600 MPa (Table 3). The computed fatigue strength is 670 MPa. The computed crack initiation area is at the specimen surface. These results are in agreement with experimental results.

5. Discussion

The previous calculations illustrate the importance of the residual stress consideration below the surface and the importance of considering their multiaxial nature and distribution (Fig. 9) for an accurate high-cycle fatigue strength assessment.

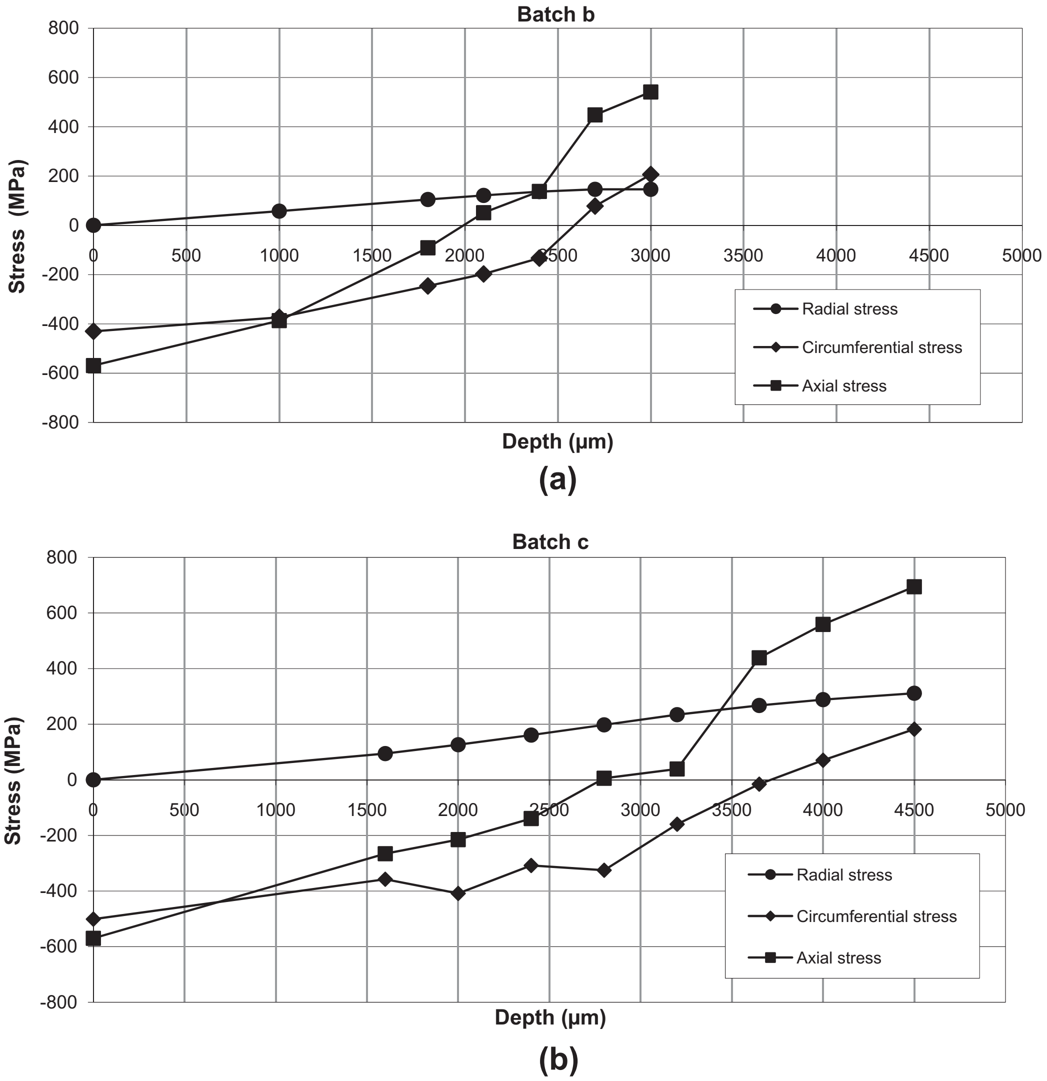

Fig. 11. Comparison of the distribution of residual stresses (measured corrected values) versus depth on specimens of (a) batch b and (b) batch c.

It is obvious that the increase in fatigue strength due to SIH treatment is cause by both the residual stresses and the high mechanical characteristics of the heat-treated layer (martensite). The authors have shown in Ref. [10] the thin microstructure of the martensite layer and its very good mechanical characteristics compared to the ferritic–pearlitic base material. This is why the fatigue strength of the martensite layer is significantly higher than that of the base material (see dashed lines in Fig. 10). However, focusing on the high characteristics of martensite is not enough for designing against fatigue. Previously, it has been shown that the best fatigue strength among the tested specimens (in terms of nominal stress amplitude, i.e. amplitude of the bending moment) under fully reversed plane bending is obtained for batch c (SIH at large depth). Fig. 11 shows a comparison of the typical distributions of residual stresses versus depth for the two batches (b and c) of SIH specimens. The values of the residual stresses are similar at the specimen surface; however, their distributions along the radius (depth) are different: the compressive residual stresses are deeper for batch c. Consequently, for batch c, the tensile residual stresses are deeper than those of batch b; its combination with the cyclic stresses due to bending is, thus, less critical. This explains the higher fatigue strength of batch c.

There are more than 50 fatigue criteria in the literature; however, not all are sensitive to residual stresses (or normal mean stresses). It is not the aim of this paper to give a full account of the fatigue hypothesis, but the following remarks are useful. One can notice that due to the heat treatment the material state in the surface layer has a very low ductility; consequently, its fatigue strength assessment is predetermined to be well treated by the principal stress hypothesis. In such a case, another hypothesis should be used for the untreated material, due to its higher ductility. As the aim of this paper is to propose a methodology that is able to assess the fatigue strength of both the treated and untreated part of a component and for being able to estimate the potential risk of crack initiation in the core (untreated material), this hypothesis has not been tested in this work. This study has been focused on two high-cycle multiaxial fatigue criteria used in the automotive industry as examples, even though other fatigue criteria could be used.

For instance, the empirical criterion proposed by Gough and Pollard for components under combined bending and torsion is not capable of accounting for residual stresses without adding a mean stress correction based on a Haigh diagram. This is also true of the Von Mises hypothesis too. In the author's opinion, the proposals made by Papadopoulos [15] and Morel [16] should be available for components treated by SIH as they depend on the maximum hydrostatic stress (even if they are not the only ones).

6. Conclusions and prospects

A methodology has been developed and validated under plane bending to assess the multiaxial high-cycle fatigue strength of ferritic–pearlitic steel treated by surface induction hardening (SIH). It is assumed that, after SIH, the specimen is made of two materials (base and treated layer) with different fatigue properties. Furthermore, it is supposed that stabilized residual stresses can be superimposed on the stresses due to cyclic loading and that their multiaxiality is accounted for by the hydrostatic stress. It has been shown that considering the residual stress profile all along the radius of the specimen is very important for an accurate fatigue strength assessment. Indeed, there is a competition between the field of stresses due to the cyclic loading and the residual stresses inside the material. Considering only the surface residual stresses is not sufficient to design for the prevention of fatigue crack initiation.

Our proposed method gives very good results under fully-reversed four-point plane bending under both the Crossland and the Dang Van high-cycle multiaxial fatigue criteria. The proposed methodology to evaluate the fatigue strength has been validated on smooth specimens. Data obtained in this study are used by engineers to simulate the mechanical behaviour of components and to prevent fatigue failure of components. The fatigue crack initiation threshold, in the multiaxial high-cycle fatigue criterion, of both the base material and the heat-treated layer is known for the steel used in this paper. The application of the proposed methodology to notched components (e.g. crankshafts) is then possible by computing the residual stresses in the notched areas of the components and by considering these stresses (after relaxation, if any) in fatigue strength assessment calculations.

In future, experiments must be carried out on martensite. Indeed, a key point of the proposed methodology is the fatigue characterisation of the heat-treated material. Furthermore, some additional investigation should be done under combined proportional and non-proportional loadings (combined bending and torsion for instance) to validate this method under loadings representative of real stress states for components. In this case, other multiaxial fatigue criteria should be tested because of the well-known low accuracy of the Dang Van and the Crossland criteria under non-proportional loadings. Another important aspect for the validation of the proposal is the simulation of residual stress relaxation. Indeed, in the experiments reported in this paper, as there was no significant residual stress relaxation (experimental observation), the problem was simpler than one describing certain industrial components. Studies simulating residual stress relaxation after surface induction hardening must be carried out. The knowledge of stabilized residual stresses under cyclic loading is a key point for high-cycle multiaxial fatigue strength assessment. At present, due to the previously-discussed reasons, industrial uses of this proposal cannot avoid experimental validation before manufacturing components for commercial use. However, the proposal is useful for comparing several designs and reducing the number of fatigue tests required for validation purposes.

References

[1] Kristoffersen H, Vomacka P. Influence of process parameters for induction hardening on residual stresses. Mater Des 2001;22:637–44.
[2] Grum J. Measuring and analysis of residual stresses after induction hardening and grinding. Mater Sci Forum 2000;347–349:453–8.
[3] Bertini L, Fontanari V. Fatigue behaviour of induction hardened notched components. Int J Fatigue 1999;21:611–7.
[4] Melander M. Theoretical and experimental study of stationary and progressive induction hardening. J Heat Treating 1985;4:145–65.
[5] Tjernberg A. Fatigue lives for induction hardened shafts with subsurface crack initiation. Eng Failure Anal 2002;9:45–61.
[6] Peterson RE. Stress concentration factors. Wiley-Interscience Publication; 1974.
[7] Anon. X-ray diffraction residual stress techniques, metal handbook, vol. 10. ASM; 1986.
[8] Prevey PC, Mason PW. The use of X-ray diffraction to determine the triaxial stress state in cylindrical specimens. In: Ruud C, editor. Practical applications of residual stress technology. ASM; 1991.
[9] Bristiel P. Modélisation magnétothermique, métallurgique et mécanique de la trempe superficielle après chauffage par induction appliquée aux vilebrequins, PhD thesis, ENSAM CER de Bordeaux, France; 2001.
[10] Coupard D, Palin-Luc T, Bristiel P, Ji V, Dumas C. Residual stresses in surface induction hardening of steels: comparison between experiment and simulation. Mater Sci Eng A 2009;487:328–9.
[11] Moore MG, Evans WP. Mathematical correction for stress in removed layers in X-ray diffraction residual stress analysis. SAE Trans 1958;66:340–5.
[12] Dang Van K. In: McDowell DL, Ellis R, editors. Advances in multiaxial fatigue, ASTM STP 1191. Philadelphia: ASTM; 1993. p. 120–30.
[13] Brand A, Flavenot J-F, Grégoire R, Tournier C. Recueil de données technologiques sur la fatigue, CETIM, France; 1992.
[14] Crossland B. Effect of large hydrostatic pressures on the torsional fatigue strength of an alloy steel. In: Int conf on fatigue of metals. London; 1956.
[15] Papadopoulos IV. A high cycle fatigue criterion applied in biaxial and triaxial out-of-phase stress conditions. Fatigue Fract Eng Mater Struct 1995;18:79–91.
[16] Morel F. A critical plane fatigue model applied to out-of-phase bending and torsion load conditions. Fatigue Fracture Eng Mater Struct 2001;24:153–64.